Ultramicroscopy 226 (2021) 113296

Contents lists available at ScienceDirect

Ultramicroscopy

journal homepage: www.elsevier.com/locate/ultramic

Atomic resolution HOLZ-STEM imaging of atom position modulation in oxide heterostructures

Magnus Nord [a,b], Juri Barthel [c], Christopher S. Allen [d,e], Damien McGrouther [a], Angus I. Kirkland [d,e], Ian MacLaren [a,*]

[a] School of Physics and Astronomy, University of Glasgow, Glasgow G12 8QQ, UK
[b] Department of Physics, NTNU, Høgskoleringen 5, 7491, Trondheim, Norway
[c] Ernst Ruska-Centre (ER-C 2), Forschungszentrum Jülich GmbH, 52425 Jülich, Germany
[d] electron Physical Science Imaging Centre, Diamond Light Source Ltd., OX11 0DE, UK
[e] Department of Materials, University of Oxford, Parks Road, Oxford OX1 3PH, UK

A B S T R A C T

It is shown that higher order Laue zone (HOLZ) rings in high energy electron diffraction are specific to individual columns of atoms, and show different strengths, structure and radii for different atom columns along the same projection in a structure. An atomic resolution 4-dimensional STEM dataset is recorded from a <110> direction in a perovskite trilayer, where only the central $LaFeO_3$ layer should show a period doubling that gives rise to an extra HOLZ ring. Careful comparison between experiment and multislice simulations is used to understand the origins of all features in the patterns. A strong HOLZ ring is seen for the La-O columns, indicating strong La position modulation along this direction, whereas a weaker ring is seen along the O columns, and a very weak ring is seen along the Fe columns. This demonstrates that atomic resolution HOLZ-STEM is a feasible method for investigating the 3D periodicity of crystalline materials with atomic resolution.

1. Introduction

Scanning transmission electron microscopy (STEM) has had a substantial impact on the characterisation of materials. Specifically, the development of high angle annular dark field imaging facilitated simple interpretation of the image contrast which is mostly incoherent and linked to atomic number [1–3]. This, in combination with aberration correction in the probe forming system in which sub-Ångström probes are now routinely achievable [4,5], has made atomic-resolution imaging of materials a powerful tool for materials characterisation [6]. However, in aberration corrected STEM imaging, details of the atomic structure along the direction of the beam is absent. In specific cases, it has been possible to recover this using discrete tomography – taking two or more known views along different crystal axes, to reconstruct the three dimensional structure [7–10]. This is challenging, however, both in its practical implementation, and in the subsequent data reconstruction. Alternatively, for some specific problems high convergence angle ADF STEM can be used to limit the depth of field to provide limited depth resolution for isolated features or single atoms [11–14]. Advances have also been made towards resolving extended features along the direction of the electron beam using scanning confocal electron microscopy [15,16], and variable angle detection has been used to determine the vertical position of single dopants or vacancies [17,18]. Nevertheless, these techniques are best applied to isolated features rather than the variations in the regular periodicity of a crystal along the beam direction, such as positional modulations in a single column. It can sometimes be inferred that an *x-y* modulation of atom positions is due to changes along the *z*-direction from the non-roundness of individual atomic columns in projection [19–23], although the periodicity can only be recovered from other information (for instance XRD refinements of the same structure [21], or viewing the same structure from an orthogonal zone axis in atomic resolution STEM).

However, there is information in the diffraction pattern related to 3-dimensional ordering. Specifically, HOLZ rings appear in electron diffraction patterns of crystals recorded at shorter camera lengths where the curvature of the Ewald sphere causes it to intersect layers of the reciprocal lattice other than that containing the origin and central part of the diffraction pattern (the Zeroeth Order Laue Zone) [24–26]. The high angle diffraction events that form these rings arise from diffraction vectors that are a significant angle away from being perpendicular to the electron beam direction, and therefore contain information about the ordering of the crystal *along* the beam direction. It was previously theorised that it might be possible to use these to prove a period doubling along the core of a 90° partial dislocation in silicon, and simulations

* Corresponding author.
E-mail address: ian.maclaren@glasgow.ac.uk (I. MacLaren).

https://doi.org/10.1016/j.ultramic.2021.113296
Received 7 September 2020; Received in revised form 16 March 2021; Accepted 24 April 2021
Available online 1 May 2021

showed that this should be observable above the thermal diffuse scattering (TDS) background [27–29]. The first clear experimental realisation of this approach was used to show differences in ordering between two different Na columns in sodium cobaltate using STEM with the optics adjusted to ensure only a narrow angular range of scattered electrons incident onto an annular detector to record intensity fluctuations in a specific Laue zone ring [30]. Recently, we showed that the intensity in a higher order Laue zone ring could be mapped using a scanning transmission electron microscope equipped with a fast pixelated detector, revealing three dimensional crystallography in a single scan [23]. The specific advantage of using a pixelated detector is that the background high-angle scattering from the TDS and other processes can be subtracted, allowing a more quantitative link between intensity and the local variations in crystallography (such as atomic shifts) leading to the formation of a given Laue zone ring. More recently, we have published a fuller description of the processing of the four-dimensional datacube to analyse the HOLZ intensity [31,32].

In our prior work [23] using a thin epitaxial film of $LaFeO_3$ sandwiched between a $SrTiO_3$ substrate and a $La_{0.7}Sr_{0.3}MnO_3$ top layer [33, 34] we showed that an extra inner Laue zone ring was present due to unit cell doubling, and specifically because of transverse modulation of heavy La atom positions along the columns parallel to the beam direction. Combined with atomic resolution STEM imaging of the in-plane structure, we were able to reconstruct the three-dimensional crystallography of the sample from a single projection. Moreover, the strength of the Laue zone ring varied across the film, and by comparisons with simulation, it was shown that this could be used to map the magnitude of atomic movements. This demonstrated that the coupled cation modulation and oxygen octahedral tilting was suppressed by both heterointerfaces – in the case of the $SrTiO_3$ because it has an untilted structure, and in the case of the $La_{0.7}Sr_{0.3}MnO_3$ because it has an incompatible tilting pattern. However, whilst it was clear from simulations that much of the intensity in the inner Laue zone was related to A-site cation modulation, it was not experimentally determined as to how much of contribution to the different HOLZ rings came from which type of column. It was speculated that the behaviour of electrons channelling along distinct columns in the structure would lead to an observable difference in the HOLZ rings. Here we extend this previous work by performing 4D-HOLZ-STEM imaging at atomic resolution. In addition, all the column-resolved diffraction patterns have been simulated using a multislice approach at the same spatial resolution in order to provide an understanding of the origins of the features therein.

2. Experimental

The sample for this work was a bilayer thin film of $La_{0.7}Sr_{0.3}MnO_3$ (LSMO) on $LaFeO_3$ (LFO) grown on a $SrTiO_3$ (STO) substrate, prepared using a standard FIB liftout procedure as described previously [33,34]

Scanning transmission electron microscopy was performed using the JEOL ARM300F (Grand ARM) at the ePSIC facility at Diamond Light Source. The microscope was operated at 200 kV and data was recorded using a pixelated STEM approach similar to that used in our previous work [23]. The detector used was a bottom-mounted Medipix 3 Merlin-EM detector. A probe convergence angle of 22.4 mrad was used and camera length chosen to ensure that the first order Laue zone of the $SrTiO_3$ was recorded by the detector without clipping. A step size of 0.25 Å per pixel was used over a scan of 100×100 pixels, with an acquisition time per pixel of 1.3ms. File conversion from raw binary to HDF5 was carried out using the *fpd* package [35].

In order to remove projector distortions from the data a non-linear mapping was made between simulated and experimental patterns using the crossing of Laue zones and Kikuchi lines as fixed reference points in *emilys* (https://github.com/ju-bar/emilys). More detailed description of how the distortion is determined and handled is provided in the *Supplemental Information*.

For mapping the HOLZ ring strength at atomic resolution, the diffraction patterns were centred, azimuthally integrated into an intensity-angle plot, background fitted using a power law, the Laue zone intensity fitted with a Gaussian, and the integrated intensity under the Gaussian plotted [23]. All processing used the *pixStem* package* [36], which relies on the *HyperSpy* package of tools for hyperspectral data processing [37]. Representative diffraction patterns for each column type were calculated by summing 10 equivalent patterns each at the same distance from the interface (i.e. periodic averaging) to minimise the effect of noise in individual patterns. Different atomic column positions were located using Atomap [22], which is a python library which has tools for locating atom positions in atomic resolution images of crystals, refining them by Gaussian fitting in real space, and then reporting their positions and average spacings them as required when sorted by different crystal planes and directions.

Multislice simulations [38,39] of diffraction patterns were calculated using Dr Probe [40] and the triclininic model structure determined in our previous work [23] by a combination of HOLZ-STEM, atomic-resolution STEM imaging and Density function theory, using thermal vibration parameters of B(La) = 0.45 $Å^2$, B(Fe) = 0.33 $Å^2$, and B(O) = 0.6 $Å^2$[41] (further details and parameters used in the simulation are provided in *Supplemental Information*). Slices with a thickness of 1.38 Å, consistent with the atomic layer distance along the incident beam direction were used. The simulations were performed with an electron energy of 200 keV, a convergence angle of 22.4 mrad, an effective source diameter of 1 Å (FWHM), a focus spread of 5 nm, and sample thicknesses up to 70nm in steps of about 1nm. Thermal diffuse scattering was simulated according to the quantum excitation of phonons model [42] by integrating over 400 passes of a Monte-Carlo procedure picking phonon configurations and by assuming an Einstein model for thermal vibrations.

3. Results

Fig. 1a shows representative diffraction patterns from the STO, LFO and LSMO layers, with the HOLZ rings indicated, together with the HAADF (Fig. 1b) and HOLZ-STEM (Fig. 1c) images calculated from the scanned diffraction dataset. The LFO layer shows a strong inner HOLZ ring which is not present in the LSMO or STO layers (indicated by the red arrow in Fig. 1a). The HAADF image (covering 90-130 mrad) shows an atomic-resolution image for a $<110>_{cubic}$ projection of a perovskite film system grown on (111). The A-site columns are bright, B-site columns appear less bright, and the oxygen-only columns are not visible. The two layers containing La are brighter than the Sr-containing substrate. Using synthetic HOLZ ring imaging from the inner ring (arrowed red in Fig 1a), only the LFO layer produces contrast, and the HOLZ-STEM image also produces atomic-resolution contrast, especially at the A-site positions.

To explore this further, 10 equivalent stripes through the HAADF and HOLZ-STEM image were identified, each one at a crystallographic period along the boundary in height, as indicated in Fig. 1a. These were aligned and summed (periodically averaged), in order to improve signal-to-noise in the HOLZ-STEM image. Fig. 2 shows these results together with an atomic model. This shows that there is strong Laue zone contrast around the A-site atoms, although it is not as spatially localised as the HAADF scattering from the same atoms. This would suggest that probe positions slightly further from the nucleus still result in channelling that scatters strongly into the Laue zone ring. It is worth noting, in contrast to the strong A-site column contrast, that relatively little contrast is seen in the HOLZ-STEM image from B-site or O columns in the $LaFeO_3$.

Whilst there is a clear variation in the strength of the Laue zone signal with distance in the film from the top and bottom interfaces, as explored in our prior work [23], the main focus of the work in the

* In 2020, pixStem was merged with pyXem (https://pyxem.github.io/pyxem-website/). pixStem will remain available for the foreseeable future, but new developments will happen in pyXem.

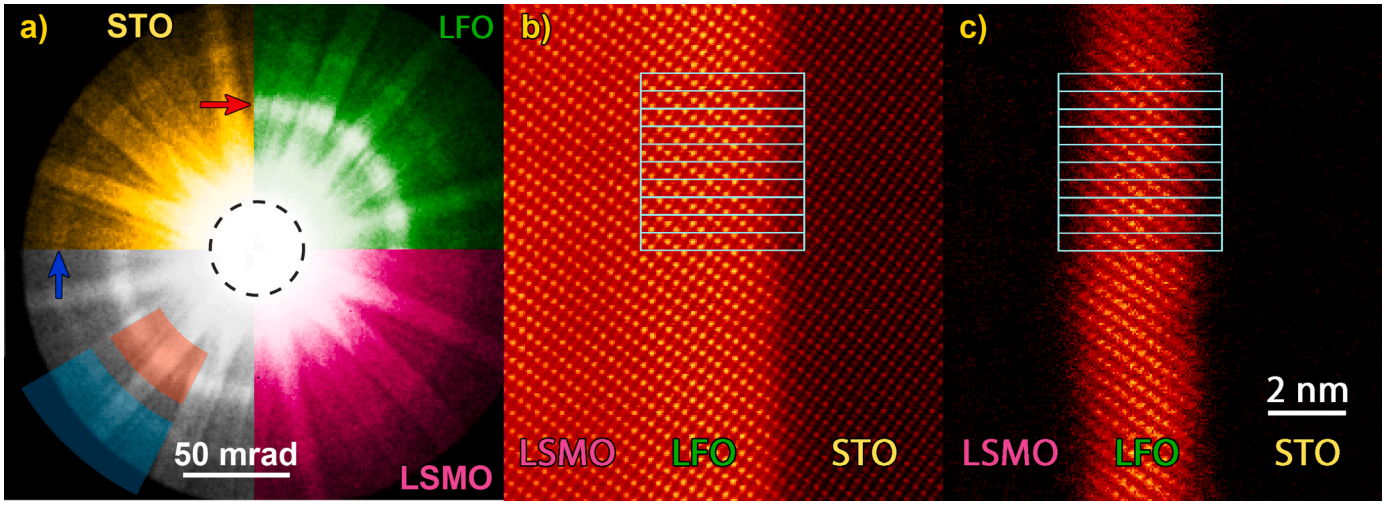

Fig. 1. Atomic resolution Laue zone imaging of a perovskite bilayer on a $SrTiO_3$ substrate: a) Composite diffraction pattern constructed from diffraction patterns taken in the STO, LFO and LSMO layers with arrows showing the positions of the two Laue zone rings (inner - red, outer - blue), as well as the size of the deliberately overexposed bright field disc as a dotted black disc; b) HAADF image (electrons scattered in the 90-130 mrad range were integrated from the scanned diffraction dataset, as shown with the pale blue arc segment in a) calculated from the scanned diffraction dataset; c) inner Laue zone intensity calculated from the scanned diffraction dataset using fitting of the decaying background and the approximately Gaussian peak for the Laue zone in the angular range indicate by the reddish segment in a). The areas averaged to create Figure 2 are indicated by the boxes.

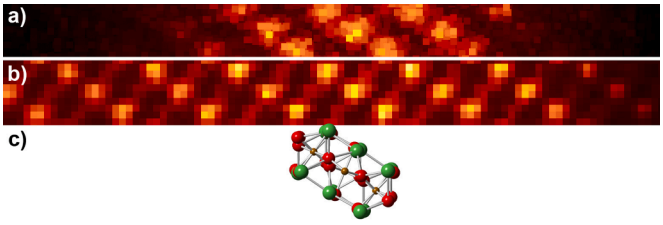

Fig. 2. Comparison of the HOLZ-STEM, the HAADF-STEM and an atomic model after periodic averaging over 10 repeats of the structure: a) Details of the inner HOLZ ring contrast; b) HAADF contrast, and c) an atomic model at the same scale (lanthanum - green, iron - brown, and oxygen - red).

present report is to investigate the details of the atomically resolved HOLZ signal. The reason for these differences in column intensities in Fig. 2 is apparent in Fig. 3a, c and e, which show average diffraction patterns summed from 10 equivalent columns in the centre of the $LaFeO_3$ layer (La-O, Fe and O columns, respectively). The La-O layer produces a strong inner first order Laue zone and a weak outer second order Laue zone indicating that there is strong modulation of the atom positions along this column, consistent with previous studies [23]. In contrast, the Fe column produces a relatively strong second order Laue zone and a weaker first order Laue one. The O column shows a better defined first order Laue zone than the Fe column (larger difference between HOLZ intensity and background intensity) and a weaker second order Laue zone. This data clearly explains why the majority of the atomic resolution contrast in Fig. 2a comes from the La-O columns, which give rise to by far the strongest of the first order Laue zones for any of the three distinct columns in this projection. This confirms one of the key conclusions of our previous work, that the main cause for the extra Laue zone was from the lateral modulation of A-site columns with a period of two primitive unit cells along the beam direction [23].

Fg. 3b, d, and f show simulated diffraction patterns. The best match to the features observed in the bright field were found simultaneously for all three probe positions when assuming a crystal thickness of 60 nm in simulations. The simulations appear sharper than the experimental patterns, especially at higher angles, but all the key features of the patterns summarised above are reproduced, indicating that our understanding of the structure and formation of the high angle electron scattering is correct. It should be noted that the experimental patterns also show significantly more diffuse scattering intensity than the simulated ones. All these effects will be considered in the following paragraphs.

Some blurring of the experimental diffraction patterns is most likely introduced by the detector point spread but this effect was included in the simulations, and the degree of blurring was matched to the contrast in the bright field disc (as detailed in *Supplemental Information*), and these are the versions shown in Fig. 3.

Nevertheless, the contrast at high angles is still significantly more blurred than in the simulations (and this is detailed more in *Supplemental Information*). A detailed comparison of the simulations and the experiments is shown in Fig. 4 in the form of traces of the integrated intensity as a function of scattering angle. It should also be noted that although the azimuthally integrated La-column signal does not clearly show the splitting seen in the simulations, it is still wider than that for the Fe and O columns. Moreover, some single line traces through the experimental data do show that the splitting is there, even if rather obscured by the blurring in the experimental patterns in this angular range discussed above. One possible reason for this is aberrations of the projector lens optics at higher angles (especially in the presence of some inelastic scattering) [43,44]. This could cause direct blurring through the strong chromatic aberration at higher angles for those projector lenses on electrons that lost small amounts of energy to plasmon interactions as well as being scattered to high angles [44]. Also, very high angle scattering sometimes appears at positions on a diffraction pattern expected for lower angle scattering due to “aberration fold-over” as discussed previously, which would overlay the high angle scattering with additional unexpected intensity [43]. This may well be a feature of the design of the STEM camera length programme, which may not be optimised for perfect diffraction pattern focus at high angles, especially as a function of energy loss. In fact, getting this would be much more challenging than the work already performed by MacLaren and Craven on EELS as the angles of diffraction involved are much larger than those typically accepted into EELS spectrometers. Nevertheless, it is clear that this can be sharper using conventional TEM diffraction lens series. Consequently, if resolution of such splittings was required, whilst preserving sufficient spatial resolution for atomic resolution images, work would be needed on characterisation and design of the lens programmes for STEM to overcome this issue.

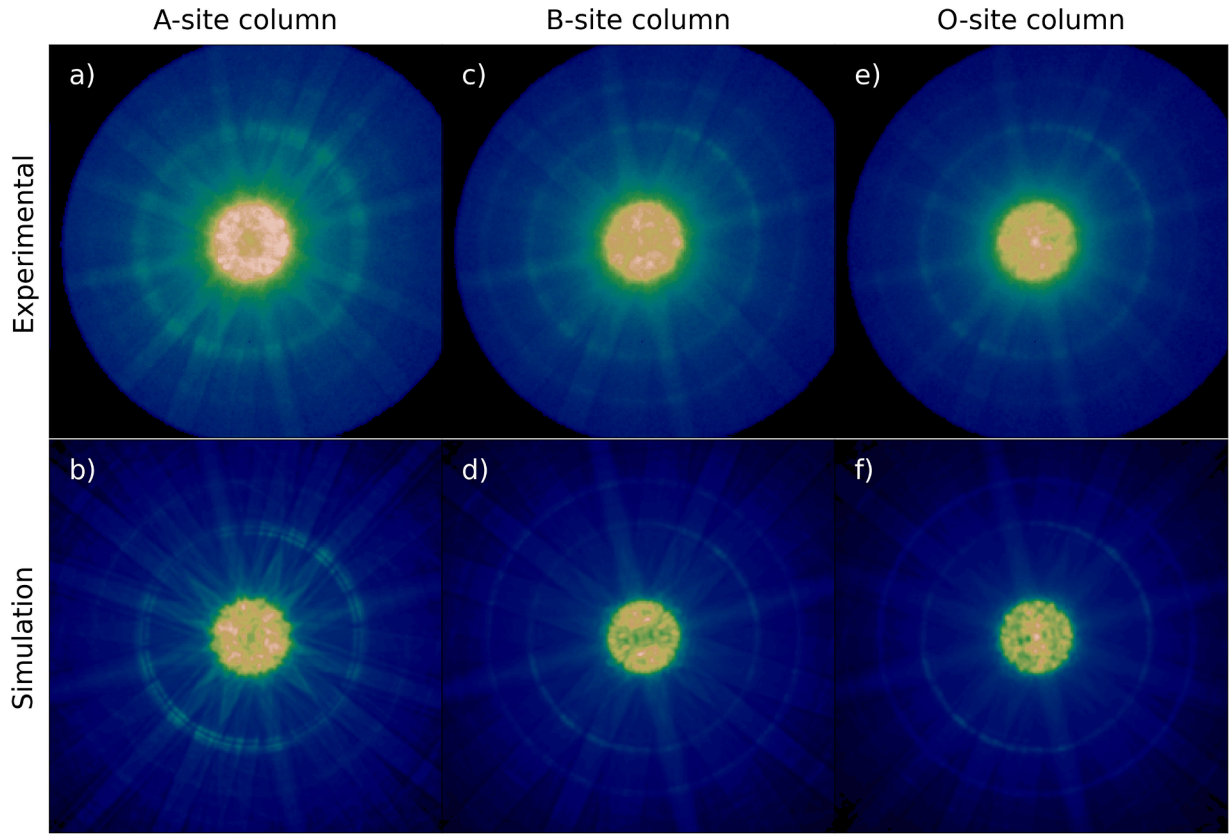

Fig. 3. Experimental (top) and simulated (bottom) diffraction patterns from the La-O (left), Fe (centre) and O (right) columns in the centre of the $LaFeO_3$ layer along the $[110]_{cubic}$ zone axis. To better see weak features in the outer parts of the diffraction pattern, the square root of the intensity is plotted.

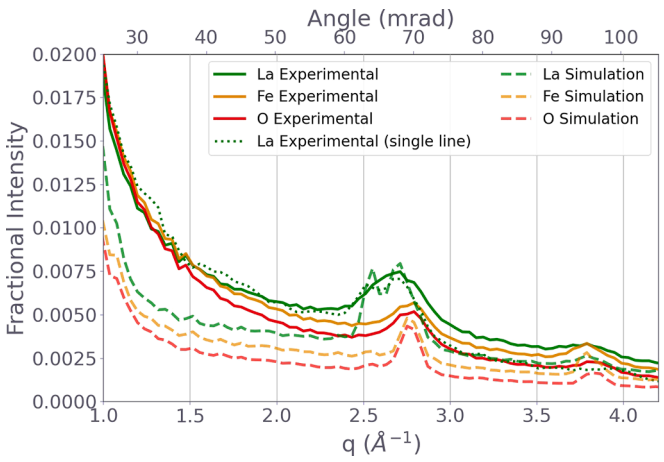

Fig. 4. Comparison of azimuthally averaged profiles for each type of atomic column in the centre of the LFO layer for experimental and simulated diffraction patterns in an angular range suitable for the first and second order Laue zones. A simple line profile is also provided for the experimental A-site data to remove the effects of blurring in the azimuthal averaging due to ellipticity of the diffraction data.

Nevertheless, despite the splitting of different rings in the same Laue zone being less clearcut than in simulations, the relative peak positions are in good agreement for all three columns between experiment and simulation, even if the signal to background is always much higher in theory than in practice. The reasons for the extra background in the experimental diffraction patterns needs further consideration. An attempt was made to include inelastic scattering due to plasmon excitations in addition to phonon excitations in the simulations by using the method proposed by Mendis [45]. While an accurate fit of the angular dependence of scattering between experiment and simulation has been shown with this approach for $SrTiO_3$ [46], the increased diffuse background at larger scattering angles observed here with $LaFeO_3$ could not be explained by low-loss inelastic scattering. Further investigation of the effects of plasmon scattering could be performed using a TEM equipped with an energy filter, although getting a low enough camera length to go out to such high angles in a diffraction pattern using a post-column filter would not be straightforward, and there are rather few in-column filter microscopes in service now (which do make high angles easier to access in an energy filtered diffraction pattern). Nevertheless, this is likely to be a minor effect and not the major reason for the observed mismatch.

Chemical disorder is unlikely to be a significant effect as the layer is pure $LaFeO_3$ and does not contain any columns with a mixture of different cations.

Instead we suggest that the sample has surface damage from FIB preparation which would add a layer of amorphous material that is imaged with low contrast but would add significantly to diffuse high angle scattering. From experience with ion beam preparation, especially with Ga in a Ga FIB, this is likely to be significant and probably the dominant issue. It is possible that specimens made with noble gas beams [47] or finished with them may produce less surface damage and improve the match between simulation and experiments.

The primary outcome of this work is that it is clearly demonstrated that Laue zone rings are strongly associated with individual atom columns and can be significantly different from one atom to another in the same structure and along the same crystal projection. This is reasonably modelled by the simulations used in this work. Notably, the radius of the Laue zone is significantly smaller for both of the Laue zone rings from the La-O columns than for those from the Fe or O columns. Splitting of HOLZ rings was previously observed by Peng and Gjønnes [26] and this was attributed to differences in the effective potential for two Bloch

waves, although this was for <111> in GaAs, a direction where only one type of atomic column is seen and this conclusion could be questionable. More detailed analysis was carried out by Jesson and Steeds [48] on split HOLZ rings in MoS_2 (following earlier work by Steeds *et al.* [49]) where most of the details were attributed to the complexities of dynamic diffraction for different branches of the dispersion surface [48].

Simulations show that the splitting and the difference between the HOLZ rings on the different columns in the $LaFeO_3$ is mainly due to dynamical diffraction from the whole unit cell at higher probe angles and in thicker material [24]. A complete future model will require a more subtle treatment of the effects of dynamical diffraction, using either multislice [50] or a Bloch wave approaches [26].

4. Conclusions

We have shown that it is possible to use the strength and position of Laue zone rings in scanning transmission electron microscopy recorded using a fast, pixelated detector, as an atomic resolution probe of ordering along the beam direction. Whilst this was implicit in the earlier work of Huang et al. [30], it is much more clearly demonstrated now that atomic resolution HOLZ imaging is a viable prospect for the characterisation of materials. This will be especially valuable in cases similar to the present one where the atomic position modulations along specific columns give rise to variations in the strength of the HOLZ ring with position. Details are also revealed that could not have been determined using the annular detector of Huang et al. [30], such as changes in ring radius or splitting of rings on individual columns. Such details could well turn out to be critical in determining the 3D details of a structure. Additionally, since this is an atomic resolution technique, provided the sample is thin enough, this analysis could reveal details of the periodicity along individual columns of atoms at the cores of defects as originally proposed by Koch and Spence [27,29,51] or at interfaces in oxide heterostructures.

Data and processing script availability

Both the raw data and the python scripts used to process the data is available at https://doi.org/10.5281/zenodo.4061715

Declaration of Competing Interest

The authors declare that they have no known competing financial interests or personal relationships that could have appeared to influence the work reported in this paper.

Acknowledgements

The authors acknowledge EPSRC funding of much of this work through the grant “Fast Pixel Detectors: a paradigm shift in STEM imaging” (EP/M009963/1). We thank Diamond Light Source for access and support in use of the electron Physical Science Imaging Centre (Instrument E02 and proposal number EM16952) that contributed to the results presented here. M.N. received additional support for this work from the European Union’s Horizon 2020 research and innovation programme under the Marie Skłodowska-Curie grant agreement No 838001. The Research Council of Norway (RCN) is acknowledged for funding for the FIB sample preparation via the Norwegian Micro- and Nano-Fabrication Facility, NorFab (197413/V30). The authors are grateful to Ms Suzanne Conner who did some of the initial analysis on the datasets presented here as part of her undergraduate project work at the University of Glasgow.

Supplementary materials

Supplementary material associated with this article can be found, in the online version, at doi:10.1016/j.ultramic.2021.113296.

References

[1] A.V. Crewe, J. Wall, J. Langmore, Visibility of single atoms, Science 168 (1970) 1338–1340.
[2] S.J. Pennycook, D.E. Jesson, High-resolution Z-Contrast imaging of crystals, Ultramicroscopy 37 (1991) 14–38.
[3] P. Hartel, H. Rose, C. Dinges, Conditions and reasons for incoherent imaging in STEM, Ultramicroscopy 63 (1996) 93–114.
[4] O.L. Krivanek, N. Dellby, A.R. Lupini, Towards sub-angstrom electron beams, Ultramicroscopy 78 (1999) 1–11.
[5] P.E. Batson, N. Dellby, O.L. Krivanek, Sub-angstrom resolution using aberration corrected electron optics, Nature 418 (2002) 617–620.
[6] I. MacLaren, Q.M. Ramasse, Aberration-corrected scanning transmission electron microscopy for atomic-resolution studies of functional oxides, Int. Mater. Rev. 59 (2014) 115–131.
[7] I. MacLaren, G. Richter, Structure and possible origins of stacking faults in gamma-yttrium disilicate, Philos. Mag. 89 (2009) 169–181.
[8] S. Van Aert, K.J. Batenburg, M.D. Rossell, R. Erni, G. Van Tendeloo, Three-dimensional atomic imaging of crystalline nanoparticles, Nature 470 (2011) 374–377.
[9] M.C. Scott, C.-C. Chen, M. Mecklenburg, C. Zhu, R. Xu, P. Ercius, U. Dahmen, B. C. Regan, J. Miao, Electron tomography at 2.4-ångström resolution, Nature 483 (2012) 444.
[10] I. MacLaren, L.Q. Wang, O. Morris, A.J. Craven, R.L. Stamps, B. Schaffer, Q. M. Ramasse, S. Miao, K. Kalantari, I. Sterianou, I.M. Reaney, Local stabilisation of polar order at charged antiphase boundaries in antiferroelectric $(Bi_{0.85}Nd_{0.15})(Ti_{0.1}Fe_{0.9})O_3$, APL Mater. 1 (2013), 021102.
[11] K. van Benthem, A.R. Lupini, M. Kim, H.S. Baik, S. Doh, J.-H. Lee, M.P. Oxley, S. D. Findlay, L.J. Allen, J.T. Luck, S.J. Pennycook, Three-dimensional imaging of individual hafnium atoms inside a semiconductor device, Appl. Phys. Lett. 87 (2005), 034104.
[12] K. van Benthem, A.R. Lupini, M.P. Oxley, S.D. Findlay, L.J. Allen, S.J. Pennycook, Three-dimensional ADF imaging of individual atoms by through-focal series scanning transmission electron microscopy, Ultramicroscopy 106 (2006) 1062–1068.
[13] G. Behan, P.D. Nellist, Optical depth sectioning in the aberration-corrected scanning transmission and scanning confocal electron microscope, J. Phys.: Conf. Ser. 126 (2008), 012083.
[14] J.G. Lozano, H. Yang, M.P. Guerrero-Lebrero, A.J. D'Alfonso, A. Yasuhara, E. Okunishi, S. Zhang, C.J. Humphreys, L.J. Allen, P.L. Galindo, P.B. Hirsch, P. D. Nellist, Direct observation of depth-dependent atomic displacements associated with dislocations in gallium nitride, Phys. Rev. Lett. 113 (2014), 135503.
[15] P. Wang, A.J. D'Alfonso, A. Hashimoto, A.J. Morgan, M. Takeguchi, K. Mitsuishi, M. Shimojo, A.I. Kirkland, L.J. Allen, P.D. Nellist, Contrast in atomically resolved EF-SCEM imaging, Ultramicroscopy 134 (2013) 185–192.
[16] P. Wang, G. Behan, M. Takeguchi, A. Hashimoto, K. Mitsuishi, M. Shimojo, A. I. Kirkland, P.D. Nellist, Nanoscale energy-filtered scanning confocal electron microscopy using a double-aberration-corrected transmission electron microscope, Phys. Rev. Lett. 104 (2010), 200801.
[17] H. Kim, J.Y. Zhang, S. Raghavan, S. Stemmer, Direct observation of Sr vacancies in $SrTiO_3$ by quantitative scanning transmission electron microscopy, Phys. Rev. X 6 (2016), 041063.
[18] J.Y. Zhang, J. Hwang, B.J. Isaac, S. Stemmer, Variable-angle high-angle annular dark-field imaging: application to three-dimensional dopant atom profiling, Sci. Rep.-UK 5 (2015) 12419.
[19] A. Borisevich, O.S. Ovchinnikov, H.J. Chang, M.P. Oxley, P. Yu, J. Seidel, E. A. Eliseev, A.N. Morozovska, R. Ramesh, S.J. Pennycook, S.V. Kalinin, Mapping octahedral tilts and polarization across a domain Wall in $BiFeO_3$ from Z-contrast scanning transmission electron microscopy image atomic column shape analysis, ACS Nano 4 (2010) 6071–6079.
[20] Q. He, R. Ishikawa, A.R. Lupini, L. Qiao, E.J. Moon, O. Ovchinnikov, S.J. May, M. D. Biegalski, A.Y. Borisevich, Towards 3D mapping of BO_6 octahedron rotations at perovskite heterointerfaces, unit cell by unit cell, ACS Nano 9 (2015) 8412–8419.
[21] F. Azough, R.I. Cernik, B. Schaffer, D. Kepaptsoglou, Q.M. Ramasse, M. Bigatti, A. Ali, I. MacLaren, J. Barthel, M. Molinari, J.D. Baran, S.C. Parker, R. Freer, Tungsten Bronze barium neodymium titanate $(Ba_{6-3n}Nd_{8+2n}Ti_{18}O_{54})$: an intrinsic nanostructured material and its defect distribution, Inorg. Chem. 55 (2016) 3338–3350.
[22] M. Nord, P.E. Vullum, I. MacLaren, T. Tybell, R. Holmestad, Atomap: a new software tool for the automated analysis of atomic resolution images using two-dimensional Gaussian fitting, Adv. Struct. Chem. Imaging 3 (2017) 9.
[23] M. Nord, A. Ross, D. McGrouther, J. Barthel, M. Moreau, I. Hallsteinsen, T. Tybell, I. MacLaren, Three-dimensional subnanoscale imaging of unit cell doubling due to octahedral tilting and cation modulation in strained perovskite thin films, Phys. Rev. Mater. 3 (2019), 063605.
[24] A.G. Emslie, Scattering of Electrons by Stibnite and Galena, Phys. Rev. 45 (1934) 43–46.
[25] P.M. Jones, G.M. Rackham, J.W. Steeds, Higher-order laue zone effects in electron-diffraction and their use in lattice-parameter determination, Proc. R. Soc. London Ser. A-Math. Phys. Eng. Sci. 354 (1977), 197-&.
[26] L.M. Peng, J.K. Gjønnes, Bloch-wave channeling and HOLZ effects in high-energy electron-diffraction, Acta Crystallogr A 45 (1989) 699–703.
[27] C. Koch, Determination of Core Structure Periodicity and Point Defect Density Along Dislocations, PhD Thesis, Arizona State University, 2002.
[28] J. Spence, C. Koch, Experimental evidence for dislocation core structures in silicon, Scr. Mater. 45 (2001) 1273–1278.

[29] J.C.H. Spence, C. Koch, On the measurement of dislocation core periods by nanodiffraction, Philos. Mag. B-Phys. Cond. Matter Stat. Mech. Electron. Opt. Magnet. Properties 81 (2001) 1701–1711.
[30] F.T. Huang, A. Gloter, M.W. Chu, F.C. Chou, G.J. Shu, L.K. Liu, C.H. Chen, C. Colliex, Scanning transmission electron microscopy using selective high-order laue zones: three-dimensional atomic ordering in sodium cobaltate, Phys. Rev. Lett. 105 (2010), 125502.
[31] G.W. Paterson, R.W.H. Webster, A. Ross, K.A. Paton, T.A. Macgregor, D. McGrouther, I. MacLaren, M. Nord, Fast Pixelated Detectors in Scanning Transmission Electron Microscopy. Part II: Post Acquisition Data Processing, Visualisation, and Structural Characterisation, 2020 in: arXiv e-printsarXiv: 2004.02777.
[32] G.W. Paterson, R.W.H. Webster, A. Ross, K.A. Paton, T.A. Macgregor, D. McGrouther, I. MacLaren, M. Nord, Fast Pixelated Detectors in Scanning Transmission Electron Microscopy. Part II: Post Acquisition Data Processing, Visualisation, and Structural Characterisation, Microsc. Microanal, 2020, https://doi.org/10.1017/S1431927620024307.
[33] I. Hallsteinsen, M. Moreau, A. Grutter, M. Nord, P.E. Vullum, D.A. Gilbert, T. Bolstad, J.K. Grepstad, R. Holmestad, S.M. Selbach, A.T. N'Diaye, B.J. Kirby, E. Arenholz, T. Tybell, Concurrent magnetic and structural reconstructions at the interface of (111)-oriented $La_{0.7}Sr_{0.3}MnO_3/LaFeO_3$, Phys. Rev. B 94 (2016), 201115.
[34] I. Hallsteinsen, M. Nord, T. Bolstad, P.-E. Vullum, J.E. Boschker, P. Longo, R. Takahashi, R. Holmestad, M. Lippmaa, T. Tybell, Effect of Polar (111)-oriented $SrTiO_3$ on Initial Perovskite Growth, Cryst. Growth Des. 16 (2016) 2357–2362.
[35] G. Paterson, fpd, https://fpdpy.gitlab.io/fpd/, (2020).
[36] M. Nord, pixStem: Analysis of pixelated STEM data, 2020. https://pixstem.org.
[37] F. de la Peña, E. Prestat, V.T. Fauske, P. Burdet, P. Jokubauskas, M. Nord, T. Ostasevicius, K.E. MacArthur, M.C. Sarahan, D.N. Johnstone, J. Taillon, L. J.V. Migunov, A. Eljarrat, J. Caron, T. Aarholt, S. Mazzucco, M. Walls, T.J.A. Slater, F. Winkler, pquinn-dis, B. Martineau, G. Donval, R. McLeod, E.R. Hoglund, I. Alxneit, D. Lundeby, T. Henninen, L.F. Zagonel, A. Garmannslund, HyperSpy v1.5.2, doi: 10.5281/zenodo.3396791 (2019).
[38] J.M. Cowley, A.F. Moodie, The scattering of electrons by atoms and crystals .1. A new theoretical approach, Acta Crystallogr. 10 (1957) 609–619.
[39] P. Goodman, A.F. Moodie, Numerical evaluation of N-beam wave-functions in electron-scattering by multi-slice method, Acta Crystallogr. A 30 (1974) 280–290.
[40] J. Barthel, Dr. Probe: A software for high-resolution STEM image simulation, Ultramicroscopy 193 (2018) 1–11.
[41] T. Caronna, F. Fontana, I.N. Sora, R. Pelosato, Chemical synthesis and structural characterization of the substitution compound LaFe1−xCuxO3 (x=0–0.40), Mater. Chem. Phys 116 (2009) 645–648.
[42] B.D. Forbes, A.V. Martin, S.D. Findlay, A.J. D'Alfonso, L.J. Allen, Quantum mechanical model for phonon excitation in electron diffraction and imaging using a Born-Oppenheimer approximation, Phys. Rev. B 82 (2010), 104103.
[43] A.J. Craven, H. Sawada, S. McFadzean, I. MacLaren, Getting the most out of a post-column EELS spectrometer on a TEM/STEM by optimising the optical coupling, Ultramicroscopy 180 (2017) 66–80.
[44] I. MacLaren, R.B. Cummings, F. Gordon, E. Frutos-Myro, S. McFadzean, A. P. Brown, A.J. Craven, Chapter twelve - performing EELS at higher energy losses at both 80 and 200 kV, in: P.W. Hawkes, M. Hÿtch (Eds.), Advances in Imaging and Electron Physics, Elsevier, 2019, pp. 299–355.
[45] B.G. Mendis, An inelastic multislice simulation method incorporating plasmon energy losses, Ultramicroscopy 206 (2019), 112816.
[46] J. Barthel, M. Cattaneo, B.G. Mendis, S.D. Findlay, L.J. Allen, Angular dependence of fast-electron scattering from materials, Phys. Rev. B 101 (2020), 184109.
[47] I. MacLaren, M. Nord, C. Jiao, E. Yücelen, Liftout of high-quality thin sections of a perovskite oxide thin film using a xenon plasma focused ion beam microscope, Microsc. Microanal. 25 (2019) 115–118.
[48] D.E. Jesson, J.W. Steeds, An investigation of three-dimensional diffraction from 2Hb-MoS2, Philos. Mag. A 61 (1990) 363–384.
[49] J.W. Steeds, D.M. Bird, D.J. Eaglesham, S. McKernan, R. Vincent, R.L. Withers, Study of modulated structures by transmission electron microscopy, Ultramicroscopy 18 (1985) 97–110.
[50] J.C.H. Spence, J.M. Zuo, J. Lynch, On the HOLZ contribution to STEM lattice images formed using high-angle dark-field detectors, Ultramicroscopy 31 (1989) 233–240.
[51] J.C.H. Spence, H.R. Kolar, G. Hembree, C.J. Humphreys, J. Barnard, R. Datta, C. Koch, F.M. Ross, J.F. Justo, Imaging dislocation cores—the way forward, Philos. Mag. 86 (2006) 4781–4796.